

Phase stability and mechanical properties of Ta enriched TiTaNbZrMo refractory high entropy alloys

Indu Avula, Avinash Chavan, Sankha Mukherjee*, Mangal Roy*

Department of Metallurgical and Materials Engineering, Indian Institute of Technology, Kharagpur 721302, India



ARTICLE INFO

Keywords:

Refractory high entropy alloys
TiTaNbZrMo
Ta enrichment
Phase stability
Elastic & mechanical properties
Electronic structure

ABSTRACT

Herein, extensive computational modelling and experimental measurements to explore the effects of partial substitution of Ta with Ti in a series of $Ti_xTa_{2-x}NbZrMo$ ($x = 0.25, 0.5, 0.75, 1$) RHEAs to improve its mechanical properties. Density-functional theory (DFT) calculations predicted that a BCC phase is stable for these alloys and its stability improves with increasing Ta concentration. CALPHAD calculations and experimental measurements revealed that RHEA alloys consist of two BCC phases (BCC1 and BCC2). Substitution of Ti atoms with Ta atoms was found to stabilize the BCC1 and increases its volume fraction. Ta enrichment also resulted in a coarser microstructure with increased Ta segregation in BCC1, and Zr segregation in BCC2 phases which resulted in an increase in the lattice parameters for both phases. DFT calculations predicted an improvement in the magnitudes of the elastic properties, bulk hardness and strength of the RHEAs by increasing Ta concentration, which is also supported by experimental results. Crystal orbital Hamiltonian population (COHP) and density of states (DOS) calculations indicated that the improvement in properties with increasing Ta content was due to the formation of strong directional metallic bonds and a higher percentage of occupied bonding states. Existing research demonstrates that in total joint arthroplasty (TJA), ceramics and CoCrMo-alloy bearing surfaces can be replaced with TiTaNbZrMo RHEAs due to their excellent mechanical properties, wear resistance corrosion resistance, and biocompatibility. However, the preliminary advantages of the Ta-rich ($Ti_5Ta_{35}(NbZrMo)_{20}$) alloy over the equiatomic TiTaNbZrMo RHEA in mechanical properties can be a potential candidate for articulating surfaces.

1. Introduction

Currently, alumina/zirconia-based ceramics and CoCrMo alloys are used as bearing surfaces in TJA to replace the hip, knee, or shoulder joints [1]. In which ceramics are inadequate to be used as articulating surfaces owing to their brittleness [2]. On the other hand leaching of Co and Cr into the blood from CoCrMo alloys are toxic, carcinogenic to the human body, promotes inflammation, and reduces cell activity [3,4].

To overcome these limitations, several researchers have investigated and developed novel materials to replace conventional biomaterials [5–10]. Recently, a new class of alloys called high entropy alloys (HEAs) have attracted great interest owing to their superior structural and functional properties [11,12]. Among them, refractory based high entropy alloys (RHEAs) have been developed for biomedical applications by using the biocompatibility of refractory elements [13–21].

Firstly, Todai et al. [14] and Wang et al. [13] proposed an equiatomic $TiZrNbTaMo$ bio-RHEA, which exhibited high Young's modulus ($E = 153$ GPa) and compressive strength ($\sigma_y = 1390$ MPa), excellent

corrosion resistance and biocompatibility as compared to cp-Ti and Ti_6Al4V . Further, Nagase et al. [16], Hori et al. [17], and Akmal et al. [22] designed and developed non-equiatomic $TiNbTaZrMo$ bio-RHEAs with excellent strength, ductility, and superior biocompatibility than the equiatomic $TiNbTaZrMo$ RHEA.

The essential properties required for a material to be used as bearing surfaces in TJA are biocompatibility, resistance to corrosion in bodily fluids, and more importantly high hardness and stiffness to maintain good wear resistance [13,23]. According to Wang et al. [13] the hardness in the $TiZrNbTaMo$ RHEA was primarily originates from the modulus-misfit between higher shear modulus elements (Ta and Mo) and other constituents.

In a study, Wang et al. [24] concluded that the microhardness and compressive yield strength of the $TiZrNbTaMo$ alloy was linearly increases with Mo concentrations. However, some studies have shown that the addition of Mo reduces the fracture toughness and improves the brittleness, which makes difficult to fabrication of the alloys. Moreover, Hua et al. [25] showed that with the addition of Ti to the

* Corresponding authors.

E-mail addresses: sankha@metal.iitkgp.ac.in (S. Mukherjee), mroy@metal.iitkgp.ac.in (M. Roy).

equimolar TiZrNbTaMo RHEA reduces the hardness and corrosion resistance. Therefore, with substitution of Ta for Ti in equimolar TiZrNbTaMo RHEA could possibly achieve better hardness in bearing surfaces.

In addition to the substantial experiments, there are several theoretical investigations on HEAs [26–38]. For example, Dai et al. [39] and Ye et al. [40] theoretically investigated the phase stability and elastic properties of TiZrHfNb-based HEAs and those are well consistent with the available experimental results. Tong et al. [26] studied the influence of the alloying elements on the mechanical properties of NbMoTaW_x ($x = \text{Cr, Zr, V, Hf, and Re}$) RHEAs, and those are correlated with their electronic structure.

Therefore, within the scope of this work, we replace Ti with Ta with the aim to enhance mechanical and biological properties in a series of TiTaNbZrMo alloys intended for bearing surfaces in TJA. First, we create the structures of disordered alloys using the special quasi-random structures (SQS) method, then studied the phase stability of Ti_xTa_{2-x}NbZrMo ($x = 0.25, 0.5, 0.75, 1$) RHEAs by the density functional theory (DFT) and CALPHAD methods. With the experiments, the validity of theoretical results on the phase evolution was examined. Next, the corresponding elastic properties and hardness of the alloys were evaluated theoretically and validated with experiments then, those were correlated with their electronic structure. Finally, optimize the concentration with high elastic modulus, hardness, and strength for articulating surfaces in TJA.

2. Computational and experimental methods

The flow chart shown in Fig. 1 is a schematic representation of all the tools and experimental techniques used for the analysis of results mentioned in this work. Representative structures of Ti_xTa_{2-x}NbZrMo ($x = 0.25, 0.5, 0.75, 1$) RHEAs were generated by following the SQS method using the Alloy-Theoretic Automated Toolkit (ATAT) [41]. The ground state total energies, equilibrium Wigner-Seitz radii, the equilibrium bulk moduli, linear elastic constants, polycrystalline moduli and hardness of the alloys were theoretically calculated using the ‘thermo_pw’ [42] and the Quantum Espresso [43] package. The nature of the chemical bonding was analyzed by the LOBSTER (Local Orbital Basis Suite Towards Electronic-Structure Reconstruction) [44] package. Then equilibrium phase fraction plots were extracted by CALPHAD [45] with Thermo-calc software [46].

Further, to validate computational results RHEAs were prepared by TIG arc melting and microstructural and phase analysis was done by SEM and XRD. The elastic and mechanical properties were measured by

Vickers hardness tester and ultrasound phase spectroscopy. The complete details of all methods are described in below.

2.1. Computational details

2.1.1. SQS models

The SQS [47,48] method as implemented in the ‘mcsqs’ program distributed with the ATAT [41] was used to generate representative BCC ($1 \times 5 \times 4$), FCC ($1 \times 2.8 \times 3.5$), and HCP ($2 \times 2 \times 5$) structures random solid solutions of RHEAs consisting of 40 atoms, respectively. The ‘mcsqs’ program uses a Monte Carlo simulated annealing loop with an objective function ensuring that the configurational space explored is extensive. The complete details of SQS method was found in the following Ref. [49].

In ATAT, the optimized atomic configuration was chosen by allowing the correlation mismatch parameter to reach a stable value for specified sets of pair and multisite parameters. The pair correlation functions were constrained up to the sixth-nearest neighbor to match with the random solid solution [49]. Then the generated best SQS structure was used to calculate phase stability, elastic properties, and electronic properties with a DFT. Fig. 2 shows the generated SQS for the equiatomic TiTaNbZrMo RHEA.

2.1.2. DFT calculations

2.1.2.1. Theoretical calculations of the phase stability of RHEAs. In order to study the phase stability of RHEAs, the ground state total energies of the FCC and HCP phases relative to that of the BCC phase ($E_{\text{FCC(HCP)}} - E_{\text{BCC}}$), equilibrium Wigner-Seitz radii ($w = \sqrt[3]{3a^3/4\pi}, a =$

lattice parameter), the equilibrium bulk moduli and enthalpy of formation of the studied alloys were calculated. The ground state total energies, equilibrium volume, and bulk modulus of the alloys were extracted by using the Brinell-Murnaghan equation of states (EOS) [50]. The formation enthalpies of RHEAs were calculated by using the following equation: $\Delta H_f(\text{HEA}) = \frac{1}{a+b+c+d+e} [\mu(Ti_aTa_bNb_cZr_dMo_e) - a\mu(Ti) - b\mu(Ta) - c\mu(Nb) - d\mu(Zr) - e\mu(Mo)]$

where $\mu(Ti)$, $\mu(Ta)$, $\mu(Nb)$, $\mu(Zr)$, and $\mu(Mo)$ chemical potentials of Ti (HCP), Ta (BCC), Nb (BCC), Zr (HCP), and Mo (BCC) and $\mu(Ti_aTa_bNb_cZr_dMo_e)$ is the total energy of the relaxed RHEA structure.

2.1.2.2. Theoretical calculations of the elastic properties of RHEAs. The linear elastic constants (C_{ij}) of the current alloys were theoretically

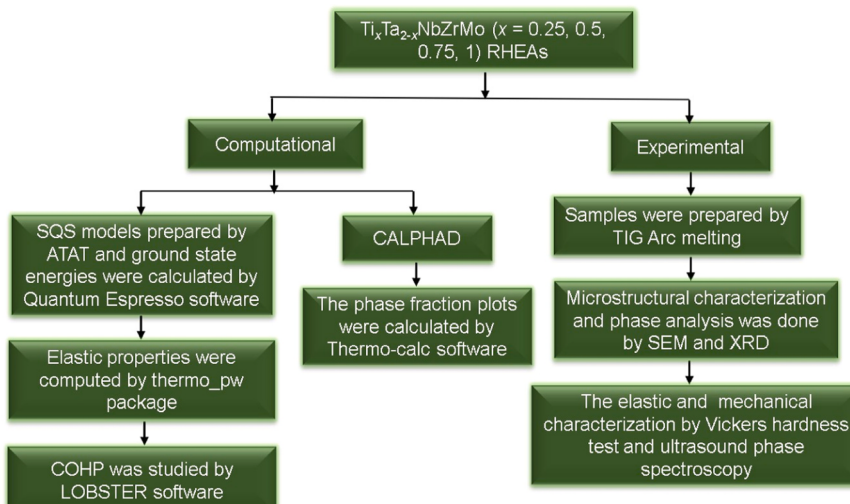


Fig. 1. A flow chart represents the overview of computational and experimental methods of RHEAs.

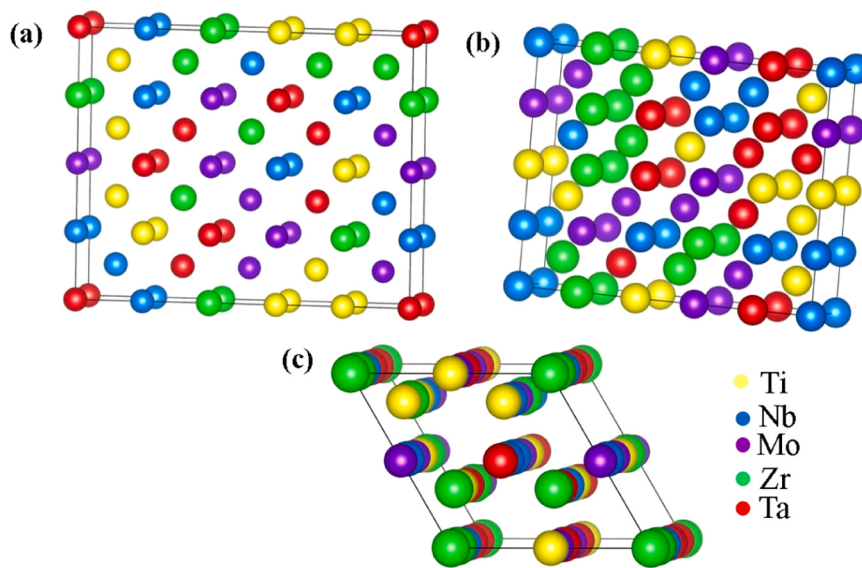


Fig. 2. The generated SQS structures for TiTaNbZrMo RHEA (a) BCC (b) FCC and (c) HCP.

calculated using the ‘thermo_pw’ [42] package. The elastic properties of a cubic system can be described by three independent elastic constants such as C_{11} , C_{12} , and C_{44} [51]. The elastic constants tensors obtained for the alloys systems using SQS exhibit lower symmetry than the cubic lattice due to the quasi-random distribution of the atomic species. Hence, we take the arithmetical average scheme and redefined elastic constants for cubic symmetry as, $C_{11} = (C_{11} + C_{22} + C_{33})/3$, $C_{12} = (C_{12} + C_{13} + C_{23})/3$, and $C_{44} = (C_{44} + C_{55} + C_{66})/3$ [52].

After getting the theoretical single-crystal elastic constants, by using Voigt-Reuss-Hill (VRH) averaging approximations [40] (shown in Supplementary Material) polycrystalline elastic properties such as bulk modulus B , shear modulus G , Elastic modulus E , and Poisson’s ratio ν were estimated. The theoretical hardness of the RHEAs were calculated by the empirical formula stated by Qiu et al. [53]: $H_v = \frac{(1-2\vartheta)E}{6(1+\vartheta)}$.

2.1.2.3. Computational settings. All DFT calculations were performed using the thermo_pw [42] and Quantum Espresso [43] packages. The projector augmented wave (PAW) [54] method was used for the calculations, and the exchange-correlation effects were described using the Perdew–Burke–Ernzerhof (PBE) functional within the generalized gradient approximation (GGA) [55].

A kinetic energy cutoff of 50 Ry for the wave function and 400 Ry for charge density computations were used for all the simulations. The convergence threshold for self-consistency through the DFT computations was 10^{-6} Ry. The convergence cutoffs for total force and total energy were kept as 10^{-5} and 10^{-6} Ry, respectively. A Monkhorst–Pack [56] k-point mesh of $6 \times 6 \times 6$ was employed for Brillouin zone (BZ) integrations for self-consistency calculations and $12 \times 12 \times 12$ k-point mesh was used for the total and partial densities of states (DOS and pDOS).

Electronic dispersion was plotted for 200 k-points along high-symmetry points of a BCC BZ. Phonon dispersion to determine dynamic stability was calculated using density-functional perturbation theory (DFPT). For electronic and phonon dispersion BZ integrations were performed using a $5 \times 4 \times 3$ k-point mesh. Further, to study the nature of chemical bonding crystal orbital Hamilton populations (COHP) [57] was used through the LOBSTER [44] package.

2.1.3. CALPHAD (calculation of phase diagram)

The equilibrium phase fraction versus temperature plots were calculated using the CALPHAD techniques [45]. The CALPHAD calculations were executed using the Thermo-Calc software with the TCHEA3 database [46].

2.2. Experimental details

2.2.1. Alloy fabrication and structure characterization

The nominal composition of $Ti_xTa_{2-x}NbZrMo$ ($x = 0.25, 0.5, 0.75, 1$) RHEAs were prepared by using Ti, Ta, Nb, Zr, and Mo elemental powders with a purity of more than 99 wt%. Arc-melted ingots were fabricated under a Ti-gettered high-purity argon atmosphere in a water-cooled copper hearth. The melted ingots were subjected to several runs of remelting and flipping to ensure chemical homogeneity. The master alloy ingots were fabricated to square ($5 \times 5 \times 5$ mm 3) shape samples using wire-cut electrical discharge machining (WEDM). Crystalline phases of the as-cast RHEAs were examined by X-ray diffraction (XRD) analysis using a Bruker D8 Advanced X-ray diffractometer with Cu K α (wavelength, $\lambda = 1.54$ Å) radiation and the 2Θ range of 30–90°. Step-scanning mode was used for scanning with a scan rate of 4° per minute. The operating voltage and current of 40 kV and 40 mA, respectively, was used for XRD. Moreover, lattice parameters of both the phases were determined using (220) diffraction line. Microstructural characterization and chemical composition of as-casted ingots was carried out by the energy dispersive spectroscopy (EDS) equipped scanning electron microscopes (SEM FEI Quanta 400 made).

2.2.2. Elastic properties characterization

The elastic constants such as the longitudinal (C_{11}) and the shear (C_{44}) wave velocities were measured along all three directions of the sample using an Ultrasound phase spectroscopy (UPS) (RAM-5000, RITEC Inc., USA) instrument. Details of the testing technique and the experimental parameters were provided in Supplementary Material. In this technique, continuous, sinusoidal, and harmonic ultrasound waves pass through the specimen and corresponding velocity (V_i) were calculated from the slope of the phase shift vs. frequency spectrum.

Once the wave velocity was measured, the respective longitudinal and shear elastic constants along the wave propagating direction could be determined by following relation: $C_{ii} = \rho V_i^2$

where ρ is the sample density. The value of the subscript ‘ i ’ lies between 1 and 3 and 4–6 for longitudinal and shear elastic constants respectively, along the three directions of the sample.

The mean value and standard deviation of measurements were reported. To determine these elastic constants, we assumed present RHEAs are isotopically polycrystalline. It is noted that isotopically polycrystalline materials have only two independent elastic constants [51], hence C_{12} was constrained by the following relation: $C_{44} = \frac{C_{11} - C_{12}}{2}$.

Further, with these elastic constants using VRH approximations we calculated the polycrystalline moduli (B , G , E , and ν) of the RHEAs.

2.2.3. Mechanical characterization

Next, the hardness of the as-casted alloys was measured using a LECO® LV700 Vickers hardness tester equipped with a 136° Vickers diamond pyramid under 200 g load and a dwell time of 15 s. A minimum of 20 indentations were taken at random sites of the ingots and the average values of hardness as well as corresponding standard deviations were reported in the results section. Moreover, the residual imprints of the indents were imaged using optical microscopy (AXIO Imager.A2m) in the differential interference contrast (DIC) mode.

3. Results

3.1. Phase stability of RHEAs by DFT calculations

Prior, to DFT calculations accuracy of the generated SQS of each RHEAs were assessed (details in [Supplementary Material](#)). The effect of Ti and Ta content on the phase stability of $Ti_xTa_{2-x}NbZrMo$ RHEAs were shown in [Fig. 3a-c](#). In [Fig. 3a](#), the energy difference of the FCC (HCP) phase relative to the BCC phase is positive, which indicates BCC phase is energetically stable. Moreover, increased Ta content in place of Ti increasingly stabilizes the BCC phase. Further BCC phase has a lower Wigner-Seitz radius and higher bulk modulus compared to FCC and HPC phases ([Fig. 3b-c](#)) indicative of larger volumes in FCC and HPC structures than the equilibrium volume. Hence FCC and HPC phases are unstable for present RHEAs.

Dai et al. [39] showed that $TiZrHfNb$ -based RHEAs follow d -occupation (d – occupation number, $n_d = \sum_{i=1}^n c_i (n_d)_i$) theory by Skriver. They determined that when $1 \leq n_d \leq 2$ and $6 \leq n_d \leq 7$ hcp phase and when $8.5 \leq n_d \leq 10$ fcc phase is the most stable, otherwise BCC phase was found to be energetically favoured. Current RHEAs average n_d (3.05

$\leq n_d \leq 3.35$) are within the stable BCC zone reflecting that BCC phase is stable over FCC or HCP phases. This is in agreement with above predictions; therefore, we used BCC phase SQS for further study.

Furthermore, the enthalpies of formation (ΔH_f) for Ta concentrations ($1 \leq x \leq 1.75$) calculated by Eq. 1 was shown in [Fig. 3d](#). The enthalpies of formation, are negative and close to zero suggesting that the RHEAs are stable solid solutions. Further, the phonon dispersion structure of RHEAs ([Fig. 4](#)) has only positive-definite modes with no imaginary frequencies indicating all the alloys are dynamically stable. All the above results conclude that the BCC phase is stable for current RHEAs and their stability increases with Ta concentration. Moreover, present alloy systems are dynamically stable at different Ta concentrations.

3.2. Phase stability of RHEAs by CALPHAD calculations

The CALPHAD-assessed equilibrium volume fraction of phase versus temperature plots ([Fig. 5](#)) for present RHEAs are predicted to be a single-phase BCC at higher temperatures. However, as temperature decreases, the BCC phase is decomposed into two BCC phases. The BCC1 and BCC2 temperatures (liquidus, solidus and decomposition), composition and volume fraction are shown detailed in [Supplementary Material](#).

3.3. Phase and Microstructure analysis of as-casted $Ti_xTa_{2-x}NbZrMo$ alloys

The X-ray diffractograms as shown in [Fig. 6a](#), reveals the $Ti_xTa_{2-x}NbZrMo$ ($x = 0.25, 0.5, 0.75$, and 1) RHEAs consist of two BCC phases (labelled as BCC1 and BCC2) without any intermetallic compound phase or ordered phase. The line profiles of the individual BCC phases were deconvoluted with the Lorentz function, and is shown for (220) diffraction line in [Fig. 6b](#) to determine the volume fraction (V_f) of each phase. [Fig. 7a](#) shows the V_f of the BCC1 phase increases, accompanied by a reduction of the BCC2 phase similar to the CALPHAD predictions (shown in [Fig. S1a](#)). The present results of equiatomic $TiTaNbZrMo$

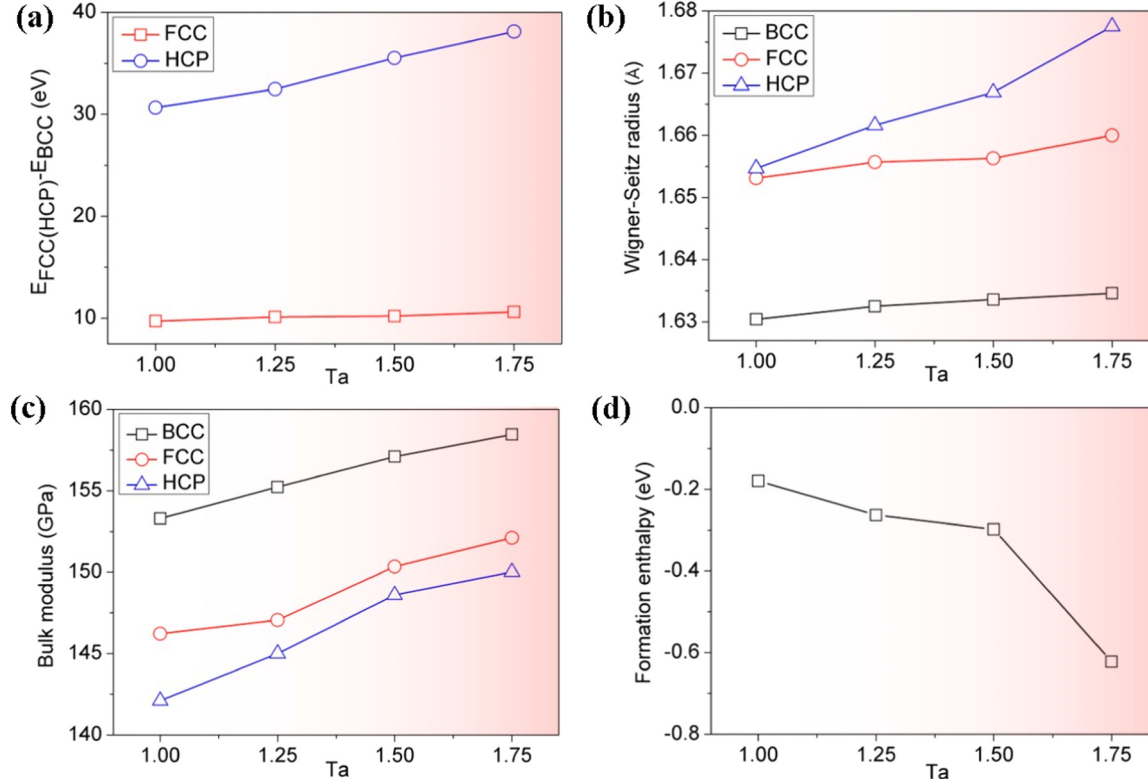


Fig. 3. The theoretically calculated (a) total energies of the FCC (HCP) phase relative to the BCC phase ($E_{FCC(HCP)}-E_{BCC}$). (b) equilibrium Wigner-Seitz radii (c) equilibrium bulk moduli and (d) enthalpy of formation for the $Ti_xTa_{2-x}NbZrMo$ RHEAs as a function of Ta content.

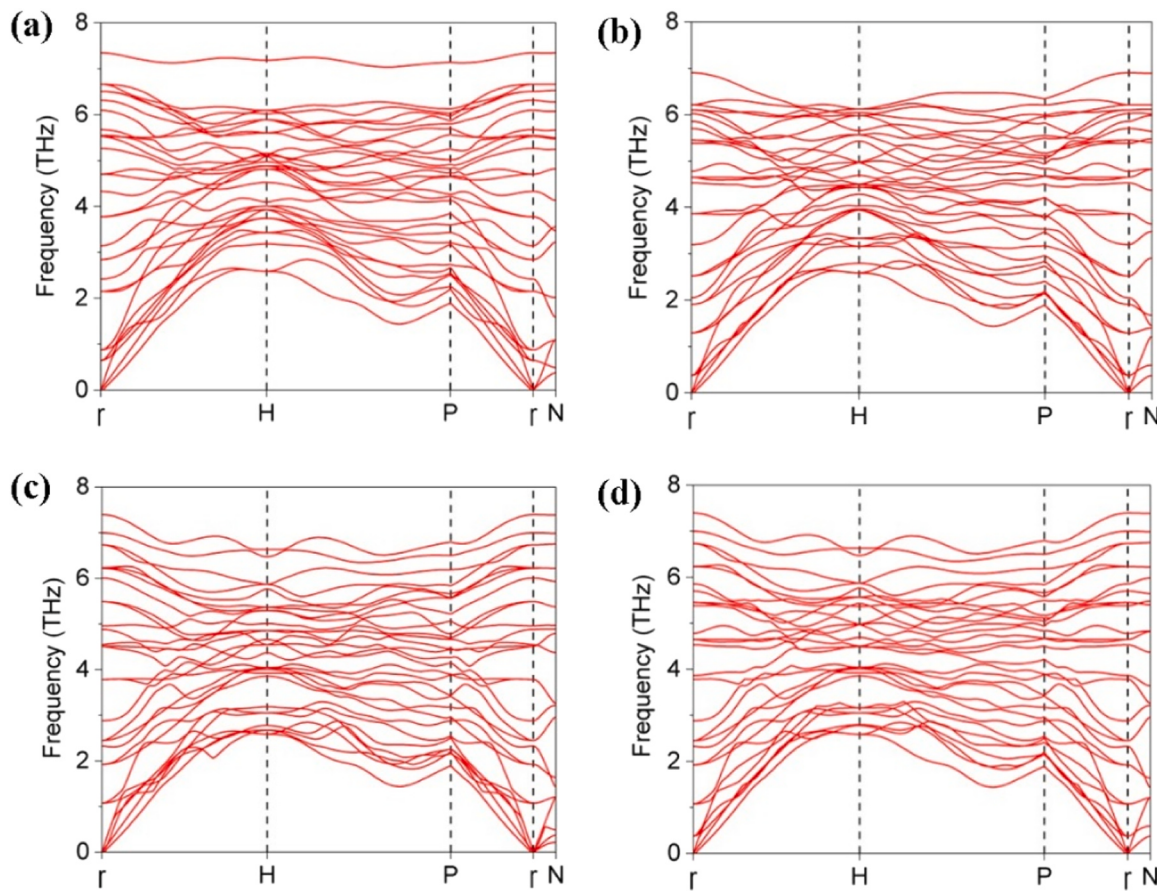


Fig. 4. The theoretically calculated phonon dispersion curves for the (a) Ta_1 (b) $\text{Ta}_{1.25}$ (c) $\text{Ta}_{1.5}$ and (d) $\text{Ta}_{1.75}$ RHEAs along high-symmetry points of a bcc Brillouin zone (G-H-P-G-N).

RHEA correlates well with the published literature [13,14,16,17,25]. Moreover, similar to as-casted ones, the TiTaNbZrMo RHEA synthesized through the mechanical alloying showed two BCC phases [58].

Moreover, the diffraction lines of BCC2 phase is appeared at lower Bragg angles, suggesting that its lattice Parameter is greater than that of the BCC1. Similarly, as the Ta concentration increases, the diffraction lines of both the phases shift towards the lower angle side (Fig. 6b), it leads to increases the lattice parameter, as shown in Fig. 7b. The lattice parameters of BCC1 (3.285 \AA) and BCC2 (3.321 \AA) phases are well mated with reported literature of as-casted (BCC1- 3.310 \AA and BCC2- 3.379 \AA) [13] and mechanical alloyed (BCC1- 3.19 \AA and BCC2- 3.43 \AA) [58] of present equiatomic RHEA. When Ti is replaced by Ta the theoretical results and mixing lattice constants exhibits a similar trend to the measured ones as shown in Fig. 7c.

The backscattered SEM micrographs of the as-casted alloys are shown in Fig. 8. composed of the light-contrast dendrites and dark-contrast interdendritic regions. The chemical composition of both the regions were quantitatively measured by EDS technique (shown in Table S4 and S5) shows that for equiatomic alloy dendrite arms are enriched with high melting point elements such as Ta, Nb, and Mo, whereas interdendrite regions are enriched with lower melting point elements as Ti and Zr. Such features in microstructure and elemental inhomogeneity are similar to the previous literatures [13,14,16,17,25].

Moreover, with increasing Ta concentration, Ta is segregate at the dendrite arms, while Zr enriched at the interdendrite regions. In contrast, Ti, Nb, and Mo concentrations decreases in dendritic and interdendrite regions. Moreover, the concentration of Zr and Ta in the dendritic and interdendrite regions are almost unchanged with Ta concentration (Fig. 9a-b). When Ti is replaced by Ta, the microstructure of the RHEAs changes from fine dendrite arms to coarse dendrite arms due

to the enrichment of Ta in the dendritic phase. Moreover, as indicated in [Supplemental Material Section 4](#) (in Fig. S1c) increasing the freezing temperature range with Ta concentration also leads to grain coarsening. According to lattice parameters of two BCC phases, dendritic and interdendrite regions are characterized as the BCC1 phase and BCC2 phase, respectively.

The soluble degree of elements in the dendrite (C_{dr}) and interdendrite (C_{id}) matrix could be quantitatively evaluated by the partition coefficient ($k = C_{dr}/C_{id}$) [24]. As can be seen in Fig. 9c, for present RHEAs Ta, Nb and Mo are segregated at the dendritic region having $k > 1$ while Ti and Zr are enriched in the interdendritic regions with $k < 1$. When Ta substituted for Ti the k values of Ta, Nb and Mo increase, particularly Ta. Whereas Ti and Zr elements k values decrease. This indicates enhancing elemental segregation, particularly the enrichment of Ta in dendritic regions and the segregation of Zr in interdendritic regions. When Ti is replaced by Ta, increases the segregation of large-sized Ta and Zr atoms in the BCC1 and BCC2 phases, which leads to the increase in the lattice parameter.

3.4. Theoretical assessment of elastic properties

3.4.1. Single-crystal elastic constants

As a sanity check, the linear elastic constants of the constituent elements were theoretically calculated and compared with existing literature (details in [Supplementary Material](#)). The average single-crystal elastic constants (C_{ij}) and the tetragonal shear elastic constant c' ($\frac{C_{11}-C_{12}}{2}$) of the $\text{Ti}_x\text{Ta}_{2-x}\text{NbZrMo}$ alloys calculated using DFT and measured using UPS are listed in [Table 1](#). It is clearly seen that DFT results are in good agreement with UPS measurements, with errors within 15% difference for all the alloys.

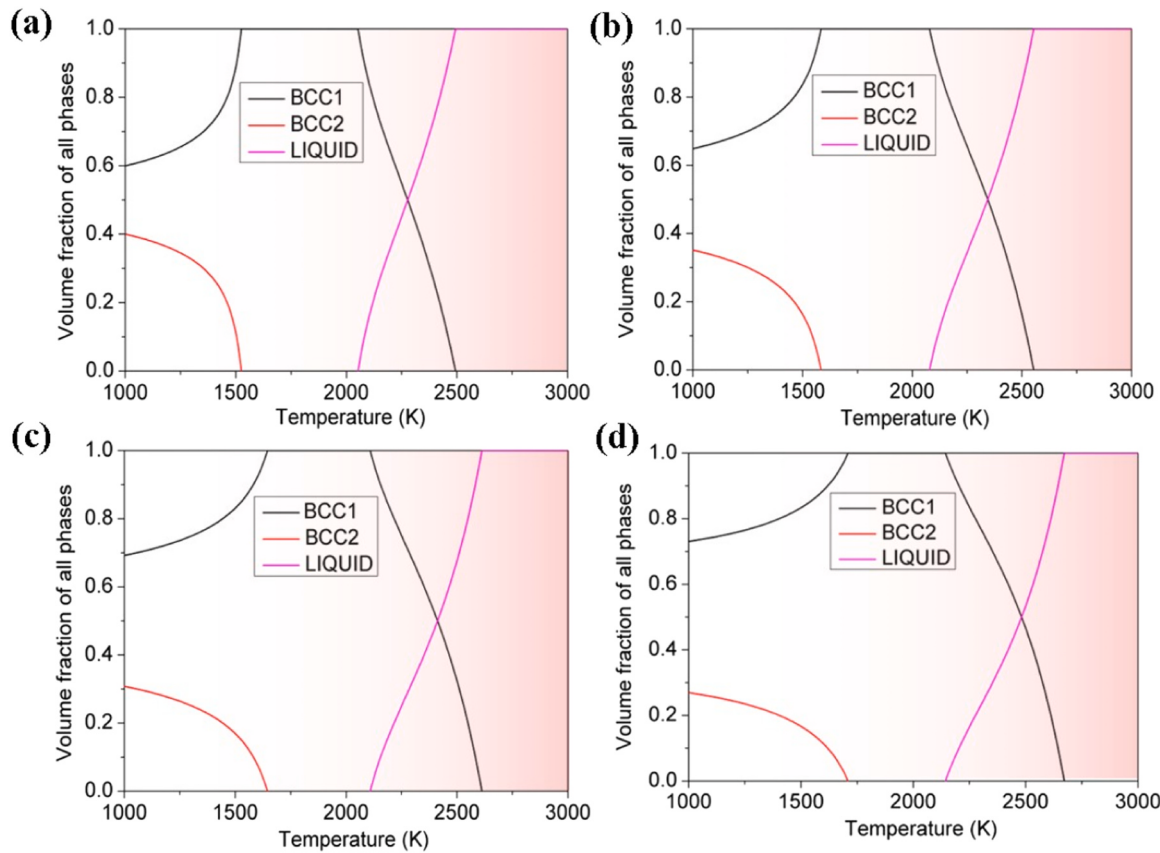


Fig. 5. The CALPHAD-assessed equilibrium phase fractions versus temperature of the (a) Ta₁ (b) Ta_{1.25} (c) Ta_{1.5} and (d) Ta_{1.75} RHEAs.

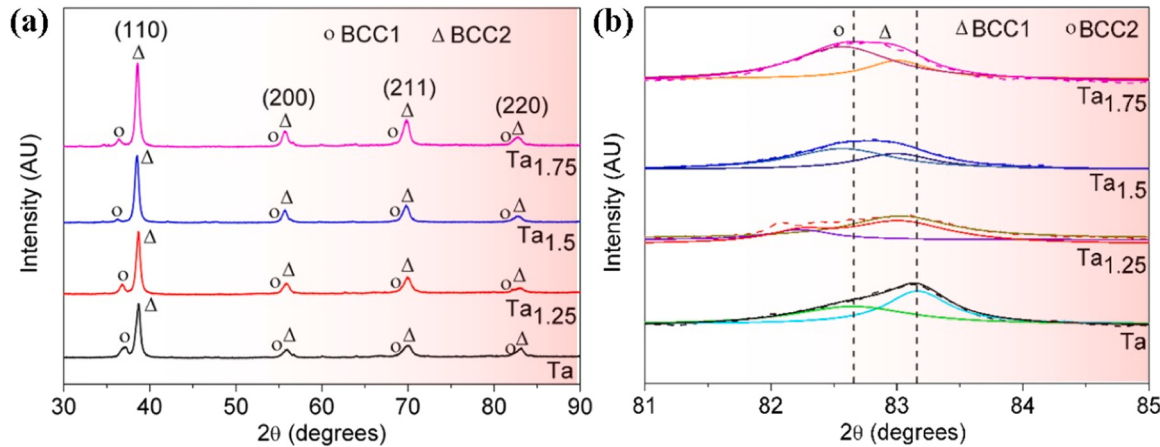


Fig. 6. XRD patterns of the arc-melted Ti_xTa_{2-x}NbZrMo RHEAs (a) Several main peaks and (b) Enlarged image of the (220) diffraction peak.

The C_{ij} and c' increases remarkably when Ti is replaced by Ta, as shown in Fig. 10a. The increasing trend of C_{11} is greater than that of C_{12} and C_{44} , while C_{12} and C_{44} are almost unchanged. The highest c' value with the addition of Ta suggests, the elastic stability of the BCC phase against tetragonal shear deformation is higher. Note that the C_{ij} of Ti_xTa_{2-x}NbZrMo alloys satisfy the Born-Huang dynamic stability criteria ($C_{11} > |C_{12}|$, $C_{11} + 2C_{12} > 0$, and $C_{44} > 0$ $C_{11}, C_{12}, C_{44} > 0$, and $C' = (C_{11} - C_{12}) / 2 > 0$) [40,59], indicates that all the RHEAs are mechanically stable as well.

3.4.2. Polycrystalline elastic properties

The polycrystalline elastic properties of the current RHEAs estimated from the DFT calculations are well matches with UPS measurements

(within 16%) and excellent consistency with the literature results [36]. As shown in Fig. 10b, with the substitution of Ti by Ta the elastic moduli of RHEAs are increasing, similar to the case of single crystal elastic constants.

The above elastic constants can also be used to predict the brittle to ductile characteristic of alloys by considering Poisson's ratio ν , Pugh's ratio (B/G), and Cauchy pressure ($CP = C_{12}-C_{44}$) [28,40,59]. The $\nu > 0.26$, $B/G > 1.75$ and larger positive values of CP reflect that materials are ductile, whereas lower values of ν , B/G and negative values of CP are associated with brittleness [28,40,59]. According to Table 1, and Fig. 10c-d the present RHEAs are ductile and their ductility decreases with Ta composition, which is consistent with the experimental observations [16,17].

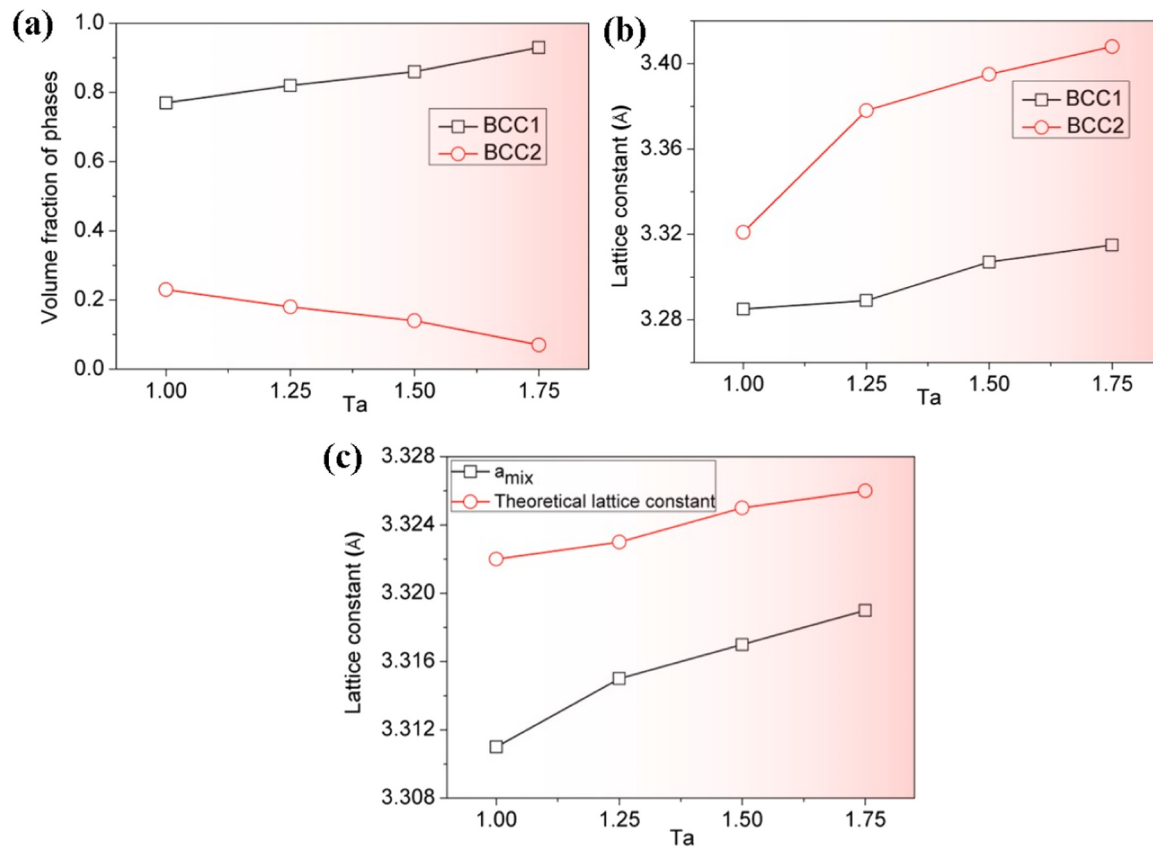


Fig. 7. (a) Volume fraction and (b) and (c) Lattice constants of $Ti_xTa_{2-x}NbZrMo$ RHEAs as function of Ta concentration.

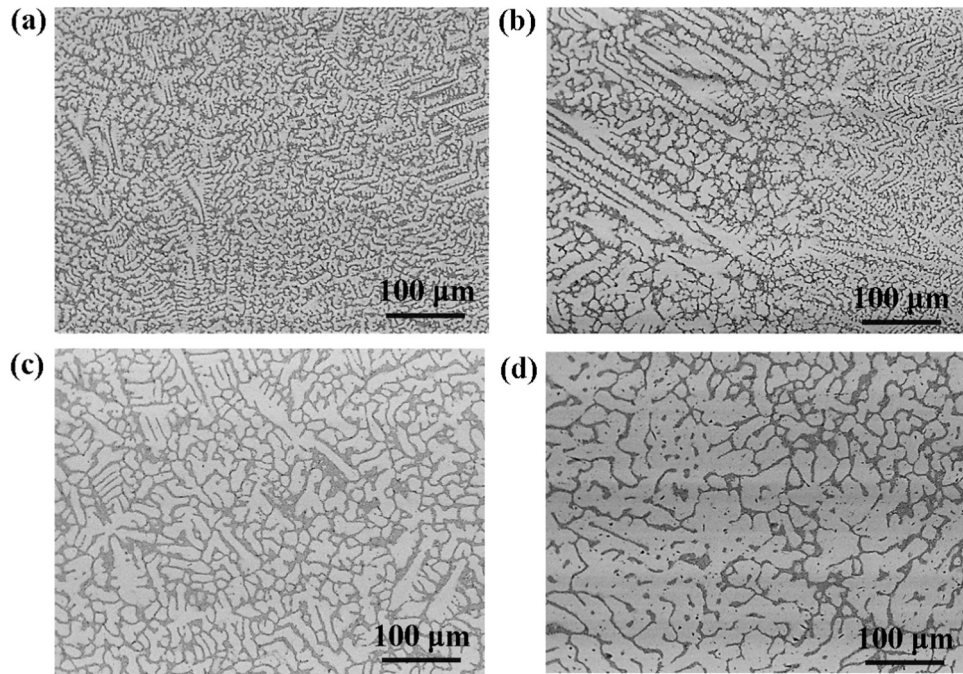


Fig. 8. SEM-BSE images of the (a) Ta₁ (b) Ta_{1.25} (c) Ta_{1.5} and (d) Ta_{1.75} RHEAs.

3.5. Experimental measurements of mechanical properties

In this study 200 g of load is used to measure the Vickers hardness because the indented area of this load covering both dendritic and inter-dendritic phases of current RHEAs (shown in Fig. S2). The hardness (H_V)

obtained from micro-Vickers indentation, calculated by the empirical formula stated by Qiu et al. [53] and rule-of mixture (H_V)_{mix} = $\sum c_i (H_{Vi})$ are mentioned in Table 2. Apparently, the measured values are well matches with the theoretical predictions within a 16% difference. Moreover, the hardness values of present RHEAs are higher than that of

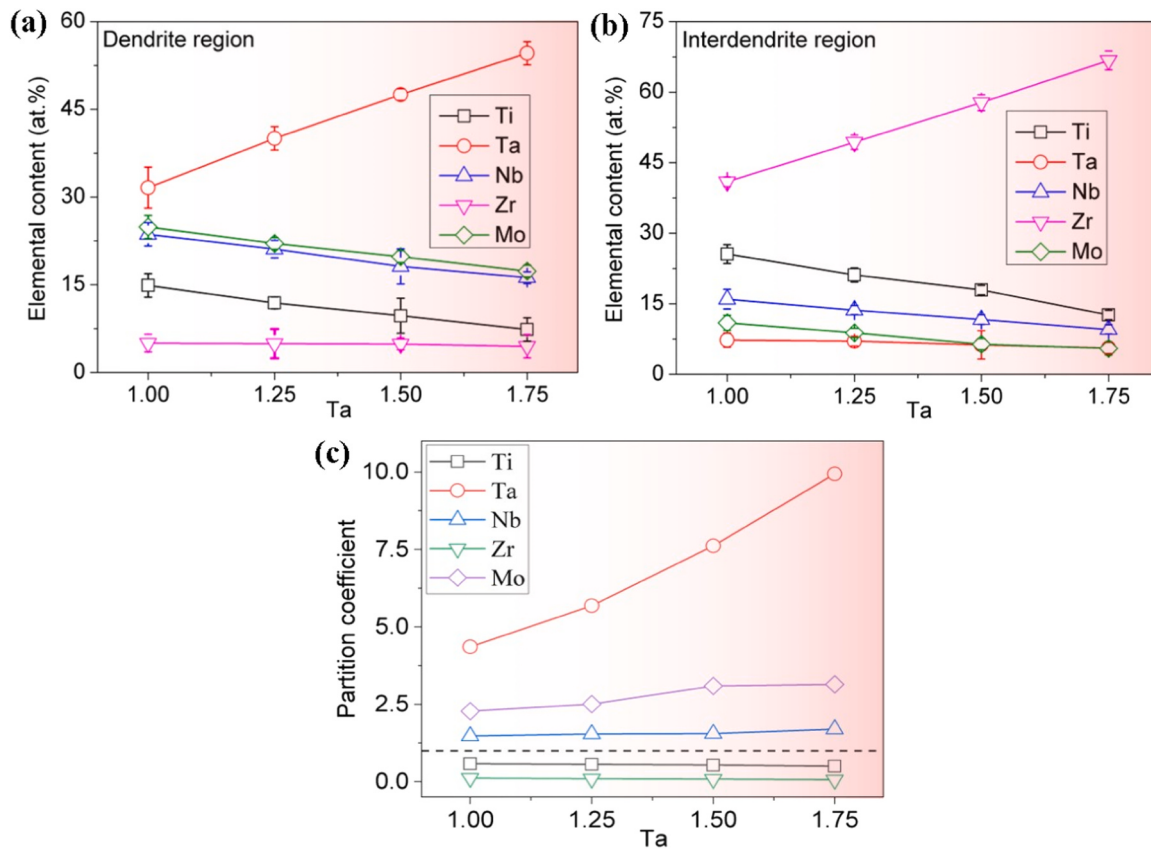


Fig. 9. Element concentration in (a) dendrite and (b) interdendrite regions for each constituent and (c) Partition coefficient of element distribution between two phases as a function of Ta concentration in Ti_xTa_{2-x}NbZrMo RHEAs.

Table 1

Single crystal elastic constants (C_{11} , C_{12} , and C_{44}), elastic moduli (G , B , E , and ν), Cauchy pressure (CP), and Pugh ratio (B/G) of the Ti_xTa_{2-x}NbZrMo RHEAs calculated from the DFT calculations and UPS measurements. The percentage differences between both are shown in parentheses.

RHEAs		C_{11} (GPa)	C_{12} (GPa)	C_{44} (GPa)	C' (GPa)	B (GPa)	G (GPa)	E (GPa)	CP (GPa)	ν	B/G
Ta	UPS	233.4 ±0.53	123.4 ±0.71	55 ±0.12	55 ±0.12	160.07 ±0.64	55 ±0.12	148.04 ±0.25	68.4 ±0.81	0.3459	2.91 ±0.02
	DFT	220.5 (5.9%)	119.7 (3.1%)	46 (15%)	50.4 (9.1%)	153.3 (4.4%)	47.71 (15%)	129.68 (14.2%)	73.7 (7.7%)	0.3590	3.213 (10.4%)
Ta_{1.25}	UPS	238.8 ±0.77	124.4 ±1.30	57.2 ±0.27	57.2 ±0.27	162.53 ±1.12	57.2 ±0.27	153.58 ±0.56	67.2 ±1.57	0.3425	2.84 ±0.04
	DFT	224.9 (5.8%)	120.4 (3.3%)	47.2 (14%)	52.25 (8.7%)	155.2 (4.7%)	49.16 (16%)	133.39 (13.1%)	73.2 (8.2%)	0.3568	3.157 (10.0%)
Ta_{1.5}	UPS	243.0 ±0.95	125.0 ±0.53	59.0 ±0.26	59.0 ±0.26	164.33 ±0.66	59.0 ±0.26	158.08 ±0.67	66.0 ±0.42	0.3397	2.79 ±0.01
	DFT	229.7 (5.5%)	120.8 (3.4%)	48 (12%)	54.45 (7.7%)	157.1 (4.4%)	50.48 (14%)	136.79 (13.4%)	72.8 (9.3%)	0.3549	3.111 (10.3%)
Ti_{1.75}	UPS	247.7 ±0.88	125.5 ±1.1	61.1 ±0.33	61.1 ±0.33	166.23 ±0.78	61.1 ±0.33	163.29 ±0.78	64.4 ±0.45	0.3362	2.72 ±0.03
	DFT	235.2 (5.1%)	120.1 (4.3%)	49 (12%)	57.55 (5.8%)	158.47 (4.7%)	52.26 (14%)	141.25 (13.5%)	71.1 (9.4%)	0.3514	3.032 (10.3%)

the CoCrMo ($H_V = 3.76$ GPa, [13]) alloys, and those can be further improved with Ta addition as shown in Fig. 11a.

However, the mixing hardness values are almost constant as a function of Ta and they are merely ~ 23% and ~ 30% of the theoretical and measured ones respectively. That means the hardness of the alloys, does not simply follow the rule of mixtures. The higher hardness in the RHEAs are likely originated from solid solution-like strengthening, rather than in a cocktail way [24,60].

3.6. Electronic structure

As shown in Fig. 12, and Fig. 13, the electronic band structure, TDOS

and PDOS of present RHEAs was calculated to study the influence of Ta content on the phase stability and mechanical performance. The red dashed horizontal line in the Fig. 12 indicates the position of the Fermi energy level (E_F). It is clearly seen that the band gap is zero due to the overlapping of the conduction band with the valence band, indicative of their metallic characteristics [61].

In Fig. 13 the black solid vertical line is the E_F and it is set to be at 0 eV. It can be seen that there is no significant difference in the TDOS of current RHEAs, which indicates there is no phase transition of RHEAs when Ti is replaced by Ta [61,62]. In the pseudogap region (a deep valley in the TDOS) [36] all the atoms almost equally contribute to the TDOS, it is showed by corresponding pDOS curves [Fig. 13]. At positive

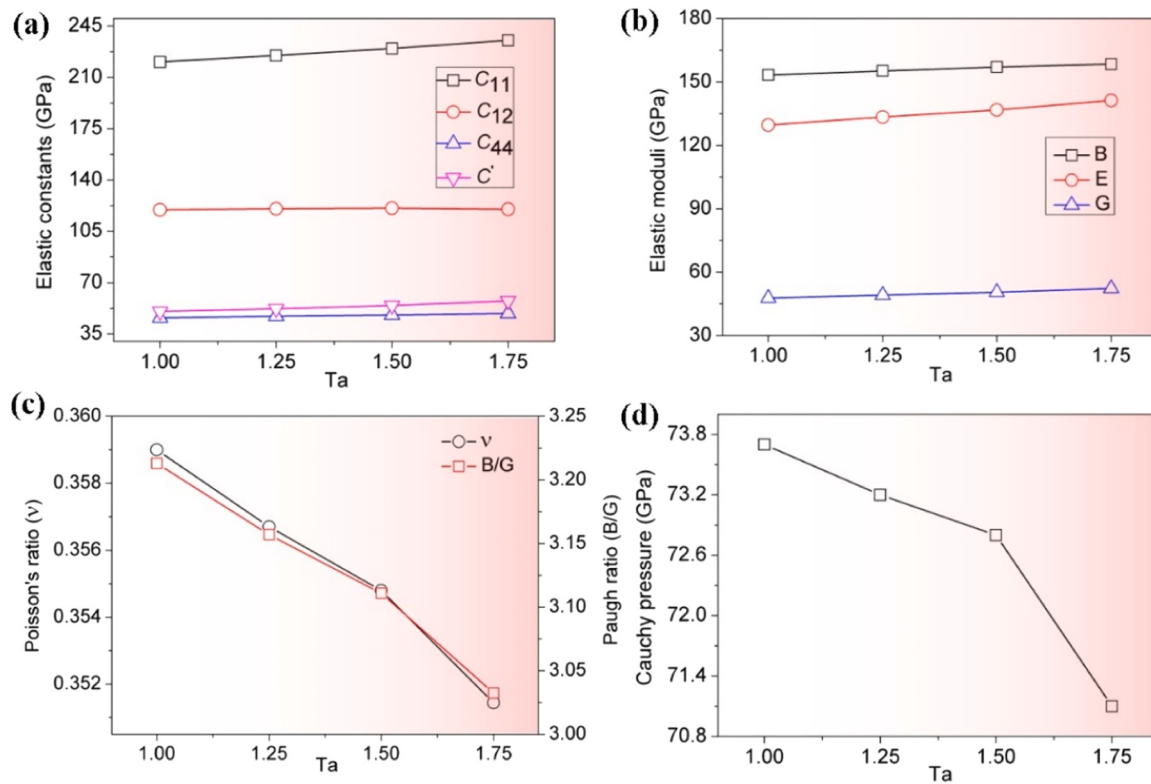


Fig. 10. The elastic constants of the $\text{Ti}_x\text{Ta}_{2-x}\text{NbZrMo}$ RHEAs (a) Single crystal elastic constants (b) Elastic moduli (c) Poisson's ratio, Paugh ration and (d) Cauchy pressure.

Table 2

The hardness of $\text{Ti}_x\text{Ta}_{2-x}\text{NbZrMo}$ RHEAs is calculated from the rule of mixtures, first principle calculations and micro-Vickers indentation. The percentage of error between theoretical and measured values are listed in the parentheses.

Hardness (H_v), GPa	$(H_v)_{mix}$	Theoretical hardness	Measured hardness
Ta	1.12	4.484 (10.4%)	4.95 ± 0.40
Ta _{1.25}	1.11	4.693 (14%)	5.34 ± 0.15
Ta _{1.5}	1.11	4.884 (16%)	5.65 ± 0.47
Ta _{1.75}	1.10	5.175 (16%)	6.02 ± 0.2

E_F , the contribution from Ti decreases and at negative E_F , the contribution from Ta increases with Ta concentration.

Usually, the pseudogap separates the bonding states from the antibonding states. As seen in Fig. 13 the E_F is lies left of the pseudogap, i.e., within the bonding states. These results clearly show that not all the bonding states are completely filled. Thus, more electrons are needed to reach the maximum structural stability in these alloys [36,63]. VEC is a dominant factor to controlling the phase stability of the alloys [64]. In this study, the VEC of $\text{Ti}_x\text{Ta}_{2-x}\text{NbZrMo}$ RHEAs increases with Ta concentration (Table S7) means an increase in the number of average electrons per atom. In this context, states at the E_F integrating towards the pseudogap leads to improves the stability with the substitution of Ti by Ta. Which is accordant to the result of energy difference of the phases and enthalpy of formation.

Further, COHP of current RHEAs were analyzed for a better understanding of obtained mechanical properties. Generally, in energy-resolved COHP plots positive and negative values are characterized by bonding and antibonding states respectively [36]. The COHP plots of the $\text{Ti}_x\text{Ta}_{2-x}\text{NbZrMo}$ RHEAs as shown in Fig. 13 reveals that the E_F is lies within the bonding states, which is consistent with DOS results.

Although the COHP plots of all the systems looks similar, one can notice that when Ti is replaced by Ta the bonding region is shifted to left with respect to the E_F . Since the number of states are different for a

different composition, we also compute the percentage of unoccupied bonding states for each composition to facilitate the comparison. The percentage of unoccupied bonding states of current RHEAs as a function of Ta are 12.8, 12.0, 11.5, and 9.8 respectively. These results clearly showed that bonding states population increases when Ti is replaced by Ta.

4. Discussion

4.1. Consistency of the observed phases evolution with empirical parameters

According to the empirical parameters (shown in [Supplementary Material](#)), all the studied alloys are expected to form a solid solution phase with a BCC structure. This observation is consistent with the results predicted by DFT. In light of these criteria, expectation of phase selection in the present RHEAs are not accord with the CALPHAD and experimental findings. It indicates, further refinement of the empirical models are need to predict the structure of RHEAs [13,24]. However, in DFT study we discuss the phase stability based on the enthalpy of formation. HEAs are enhance the stability of solid solutions due to their large entropies of mixing (ΔS_{mix}), which leads to potentially lower the mixing free energy (ΔG_{mix}). The ΔS_{mix} and ΔG_{mix} for present RHEAs require further investigations.

The present arc melted $\text{Ti}_x\text{Ta}_{2-x}\text{NbZrMo}$ RHEAs are somewhat away from the thermodynamic equilibrium state due to the rapid cooling of the melt and lack of long period of annealing for atomic diffusion to achieve chemical homogeneity. In these alloys, formation of dual phases is partially influenced by the following factors: First, during solidification segregation of constituent elements due to their large difference in the melting temperature. Second, miscibility gap in the Zr-Ta system at close to the annealing temperature [65]. These are possible reasons associated with the remarkable enrichment of Ta in BCC1 and Zr in BCC2 with Ta content [24].

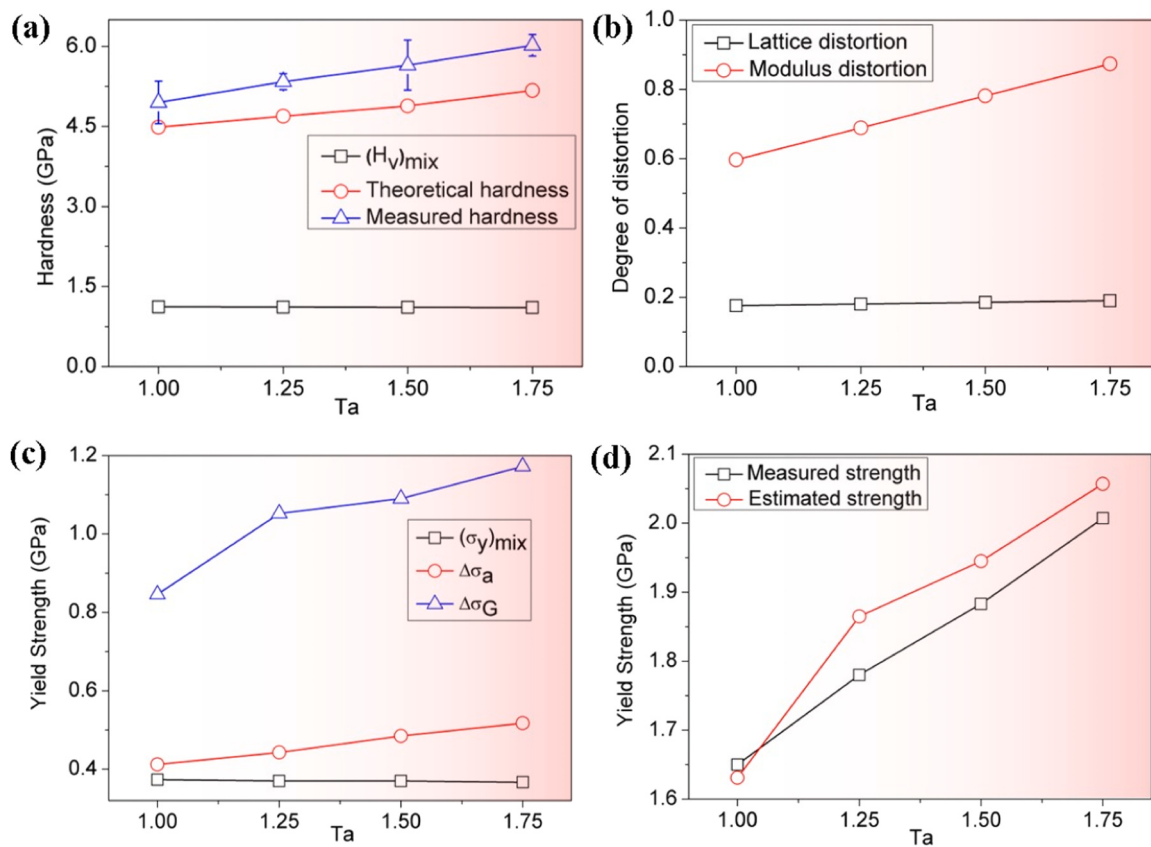


Fig. 11. (a) Hardness (b) Variation of local lattice and modulus distortions (c) and (d) Yield strength of $\text{Ti}_x\text{Ta}_{2-x}\text{NbZrMo}$ alloys as a function of Ta concentration.

4.2. Effect of replacement of Ta for Ti on elastic and mechanical properties

As indicated in Section 3.4, with the increase of Ta concentration, the elastic constants of all the RHEAs increased. The single-crystal elastic constants of the BCC structure alloys are dependent on the number of valence electrons, which increases with the increase of valence electrons [66,67]. Lobzenko et al. [68] demonstrated that elastic constants decreases when a higher valency element (Mo-group VI element) is substituted with a lower valency element (Zr-group IV element) due to the weaker metallic bonds. This hypothesis is consistent with current observations, as $\text{Ti}_x\text{Ta}_{2-x}\text{NbZrMo}$ alloys elastic constants increase due to the replacement of the lower valency element Ti (VEC-4) with the higher valency element (Ta).

The polycrystalline elastic moduli (E , B , and G), hardness and strength of the alloys are closely related to their single-crystal elastic constants. By making smaller values of C_{11} , C_{12} , and C_{44} those properties can be lower [69]. Thus, VEC is directly related to these properties. Therefore, elastic moduli (E , B , and G), hardness and strength of the alloys increases with Ta content. In a study Koval et al. [36] found that a higher VEC (4.7) phase ($\text{Ti}_{15}\text{Zr}_{10}\text{Nb}_{20}\text{Ta}_{31}\text{Mo}_{24}$) in a TiZrNbTaMo RHEA exhibited greater E and B due to the strong directional bonds compared to a lower VEC (4.4) phase ($\text{Ti}_{24}\text{Zr}_{43}\text{Nb}_{12}\text{Ta}_8\text{Mo}_{13}$).

The PDOS of each element reveals that electronic states originated from the d orbitals and they form a hybridization. The electron occupancy of the d orbitals significantly impacts the mechanical properties of materials [30,62]. With increasing Ta content, the height of the DOS peak of Ta rises significantly due to stronger hybridization between the d orbitals of Ta element with other metals. This resulting in the formation of stronger metallic bonds that enhance the mechanical properties of the alloy. The COHP analysis reveals when Ti is replaced by Ta the percentage of bonding states occupation increases, leads to improves the

mechanical properties. In a study, Koval et al. [36] found in TiZrNbTaMo alloy the phase with a higher percentage of occupied bonding states has higher B , E and H_v .

Moreover, substitution of larger Ta (atomic size and modulus) for smaller Ti in $\text{Ti}_x\text{Ta}_{2-x}\text{NbZrMo}$ RHEAs would cause misfit strain, it is a crucial factor affecting the mechanical properties of the RHEAs [24,60]. Hence the solid-solution strengthening mechanism of the RHEAs are discussed in next section.

4.3. Strengthening mechanism of RHEAs

As indicated in Section 3.5, the microhardness in the current alloys is likely originated from solid solution-like strengthening [24,60]. In RHEAs, mutual interaction between the atoms causes local elastic stress fields due to the misfit sizes or moduli. The interaction of local elastic stress fields with the dislocations stress fields during deformation arises the solid solution strengthening in metallic solid solutions [13]. The resulting misfit stress is given by the following equation: $\Delta\sigma = 0.1\mu(\delta_\mu + \beta\delta_a)^{4/3}c^{2/3}$ [60]

where μ is shear modulus (GPa), c is solute concentration, δ_μ and δ_a are the distortions from modulus misfit and lattice misfit, respectively and β is a constant this value depends on the type of dislocation. The δ_μ and δ_a calculated for current alloys are given in the Supplementary Material.

As shown in Fig. 11b, $\text{Ti}_x\text{Ta}_{2-x}\text{NbZrMo}$ RHEAs modulus distortion is three times higher than lattice distortion and its increases with Ta content. In contrary the degree of lattice distortion is almost constant. Which can be attributed to replacing of lower modulus (Ti = 44 GPa) element with a higher modulus (Ta = 69 GPa) element. Similar to the previous literature [13], in the present RHEAs also majority of strength originates from the modulus-misfit. With increasing Ta content, the degree of distortion increases by 46%, while the experimental

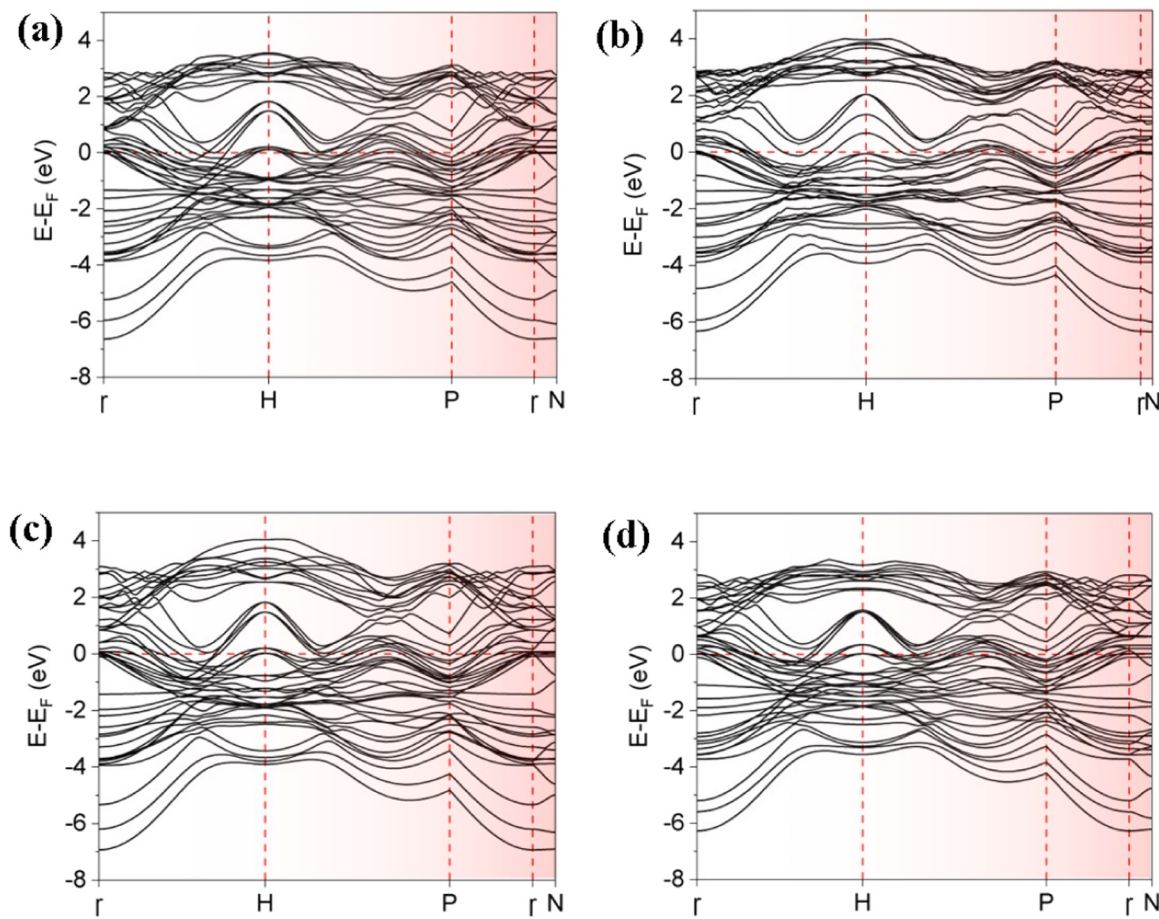


Fig. 12. Electronic band structure of (a) Ta₁ (b) Ta_{1.25} (c) Ta_{1.5} and (d) Ta_{1.75} RHEAs along high-symmetry points of a bcc Brillouin zone (G-H-P-G-N).

micro-hardness increases by 22%.

Using Tabor's relation [60], the RT yield strength (σ_y) of the RHEAs was calculated from measured Vicker's hardness and ROM hardness values are displayed in Table S11. Similar to the hardness values the ROM values are lower than the experimental values. In such a case the RT yield strength of the RHEAs are given by the following equation: $\Delta\sigma = (\sigma_y)_{mix} + \Delta\sigma_a + \Delta\sigma_\mu$ [24,60]

where $(\sigma_y)_{mix}$ is stress from the rule of mixtures, $\Delta\sigma_a$ and $\Delta\sigma_\mu$ are stress due to the lattice and modulus misfit respectively.

The yield strength estimated from the contribution of the modulus misfit $\Delta\sigma_\mu$ and lattice misfit $\Delta\sigma_a$ are shown in Fig. 11c. It can be inferred that at RT, a contribution from $\Delta\sigma_\mu$ greater than the $\Delta\sigma_a$, the result is consistent with the reported literature [13]. When Ti is replaced by Ta the $\Delta\sigma_\mu$ and $\Delta\sigma_a$ are increase however, an increasing trend is more for the $\Delta\sigma_\mu$ due to the increases of modulus distortion. Consequently, the calculated σ_y values of Ti_xTa_{2-x}NbZrMo RHEAs are agrees well with the yield strength obtained from Vickers hardness within the 5% error [Fig. 11d]. Hence, it is evident that the substitution of Ta for Ti can significantly improve its mechanical properties.

4.4. Advantages of Ta-rich RHEA (Ti₅Ta₃₅(NbZrMo)₂₀) over equiatomic RHEA

As is well known, the essential properties for bearing surfaces are high hardness and stiffness to maintain good wear resistance. In this work, the Ta-rich RHEA have higher H_V (6.02 GPa), E (163.29) and σ_y (2007 MPa) over the equiatomic TiTaNbZrMo RHEA (H_V = 4.95 GPa, E = 148.04 GPa and σ_y = 1650 MPa). Hence it can be a potential candidate for use as articulating surfaces in TJA.

However, in this study strength is not measured experimentally rather than its calculated by the measured hardness. In spite of that it is rarely used for comparisons hence subsequent studies are on-going on the tensile properties. Furthermore, wear resistance is an additional critical issue for this application. According to Khrushev [70] the wear resistance of materials is in general proportional to their Vickers hardness. In this sense, Ta-rich alloy may have higher wear-resistant than the equiatomic RHEA, which needs to be confirmed in future work. Further corrosion in simulated physiological medium and biocompatibility needs to evaluated, these are on-going study.

5. Conclusions and outlook

In the present study, with the substitution of Ta for Ti, the phase stability and mechanical properties of the Ti_xTa_{2-x}NbZrMo (x = 0.25, 0.5, 0.75, and 1) RHEAs have been exclusively investigated by the first-principles calculations and those are validated with experimental results. The key findings of this study are summarized as follows:

1. The as-cast alloys and CALPHAD predictions consist of two BCC phases and the volume fraction of BCC2 decreases with increase in Ta concentration. The phase stability of BCC increases predicted by enthalpy of formation determined through DFT calculations.
2. When Ti is replaced by Ta, the structure changes from fine to coarse dendrites due to the enrichment of Ta in the dendritic regions.
3. The theoretical calculations of elastic and mechanical properties are in excellent agreement with experimental measurements.
4. Experimental results indicate that the Vickers hardness, Young's modulus and strength increased by 22%, 10% and 22% respectively when equiatomic to Ta rich sample. This is due to the strong

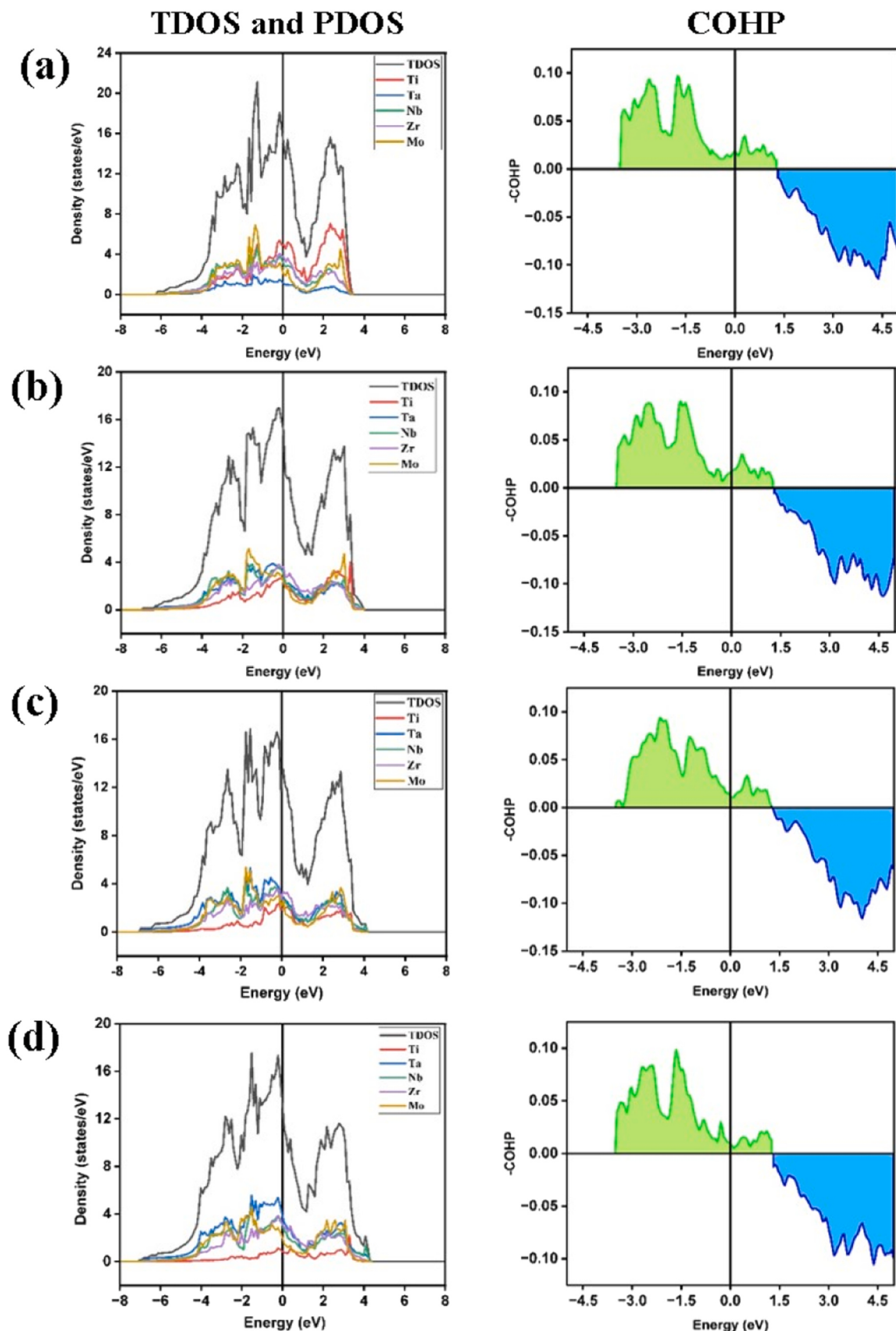


Fig. 13. TDOS, PDOS and COHP of (a) Ta_1 (b) $\text{Ta}_{1.25}$ (c) $\text{Ta}_{1.5}$ and (d) $\text{Ta}_{1.75}$ RHEAs.

directional metallic bonds, higher percentage of occupied bonding states and higher modulus misfit with Ta content.

In summary, our preliminary study on the $Ti_xTa_{2-x}NbZrMo$ RHEAs reveals the Ta-rich RHEA has good phase stability and significant mechanical properties (high hardness, high strength and high elastic modulus) than the equiatomic RHEA. In this context, it can be used as bearing surfaces in TJA.

Furthermore, our ongoing study necessitates an examination of ΔG_{mix} to study the phase stability by DFT calculation. Moreover, wear, corrosion behavior in simulated body fluid and an in-vitro and in vivo evaluation of biocompatibility are further required to use this material as bearing surfaces.

CRediT authorship contribution statement

Sankha Mukherjee: Validation, Supervision, Resources, Methodology, Conceptualization, Writing – review & editing. **Mangal Roy:** Writing – review & editing, Validation, Supervision, Resources, Methodology, Funding acquisition, Conceptualization. **Indu Avula:** Writing – original draft, Methodology, Investigation, Formal analysis, Data curation, Conceptualization. **Avinash Chavan:** Writing – review & editing, Data curation.

Declaration of Competing Interest

The authors declare that they have no known competing financial interests or personal relationships that could have appeared to influence the work reported in this paper.

Data availability

The raw/processed data required to reproduce these findings cannot be shared at this time as the data also forms part of an ongoing study.

Acknowledgements

The authors gratefully acknowledge the support for the experimental facilities at the Department of Metallurgical and Materials Engineering and the Central Research Facilities, IIT Kharagpur. The authors would like to acknowledge the National Supercomputing Mission (NSM) for providing computing resources of ‘PARAM Shakti’ at IIT Kharagpur, which is implemented by C-DAC and supported by the Ministry of Electronics and Information Technology (MeitY) and Department of Science and Technology (DST), Government of India. A.I. acknowledges the Ministry of Education (MoE), Govt. of India for the Prime Minister’s Research Fellowship (PMRF) to carry out the research.

Appendix A. Supporting information

Supplementary data associated with this article can be found in the online version at [doi:10.1016/j.jallcom.2024.174408](https://doi.org/10.1016/j.jallcom.2024.174408).

References

- [1] P.A. Dearnley, A review of metallic, ceramic and surface-treated metals used for bearing surfaces in human joint replacements, Proc. Inst. Mech. Eng., Part H J. Eng. Med. 213 (1999) 107–135, <https://doi.org/10.1243/0954411991534843>.
- [2] R. Khanna, J.L. Ong, E. Oral, R.J. Narayan, Progress in wear resistant materials for total hip arthroplasty, Coatings 7 (2017), <https://doi.org/10.3390/coatings7070099>.
- [3] J. Fisher, X.Q. Hu, J.L. Tipper, T.D. Stewart, S. Williams, M.H. Stone, C. Davies, P. Hatto, J. Bolton, M. Riley, C. Hardaker, G.H. Isaac, G. Berry, E. Ingham, An in vitro study of the reduction in wear of metal-on-metal hip prostheses using surface-engineered femoral heads, Proc. Inst. Mech. Eng., Part H J. Eng. Med. 216 (2002) 219–230, <https://doi.org/10.1243/09544110260138709>.
- [4] A.K. Madl, M. Liong, M. Kovochich, B.L. Finley, D.J. Paustenbach, G. Oberdörster, Toxicology of wear particles of cobalt-chromium alloy metal-on-metal hip implants Part I: Physicochemical properties in patient and simulator studies, Nanomed.
- Nanotechnol., Biol., Med. 11 (2015) 1201–1215, <https://doi.org/10.1016/j.nano.2014.12.005>.
- [5] H. Song, S. Lee, K. Lee, Microstructure and electrochemical behaviors of equiatomic TiMoCrZr and Ti-rich TiMoCrZr high-entropy alloys for metallic biomaterials, Arch. Metall. Mater. 65 (4) (2020), <https://doi.org/10.24425/amm.2020.133692>.
- [6] Superior antiwear biomimetic artificial joint based on high-entropy alloy coating on porous Ti6Al4V, ScienceDirect, (n.d.). <http://www.sciencedirect.com/science/article/pii/S0301679x21000852> (Accessed 23 December 2022).
- [7] D. Liu, H. Xie, Z. Ma, W. Zhang, H. Zhao, L. Ren, Simultaneous enhancement of anti-friction and wear resistance performances via porous substrate and FeCoNiTiAl high entropy alloy coating of artificial joint materials, J. Mater. Res. Technol. 19 (2022) 2907–2915, <https://doi.org/10.1016/j.jmrt.2022.06.051>.
- [8] W. Wang, K. Yang, Q. Wang, P. Dai, H. Fang, F. Wu, Q. Guo, P.K. Liaw, N. Hua, Novel Ti-Zr-Hf-Nb-Fe refractory high-entropy alloys for potential biomedical applications, J. Alloy. Compd. 906 (2022) 164383, <https://doi.org/10.1016/j.jallcom.2022.164383>.
- [9] F. Cemin, L. Luís Artico, V. Piroli, J. Andrés Yunes, C. Alejandro Figueroa, F. Alvarez, Superior in vitro biocompatibility in NbTaTiVZr(O) high-entropy metallic glass coatings for biomedical applications, Appl. Surf. Sci. 596 (2022) 153615, <https://doi.org/10.1016/j.apsusc.2022.153615>.
- [10] S. Hu, T. Li, Z. Su, S. Meng, Z. Jia, D. Liu, A novel TiZrNb medium entropy alloy (MEA) with appropriate elastic modulus for biocompatible materials, Mater. Sci. Eng. B 270 (2021) 115226, <https://doi.org/10.1016/j.mseb.2021.115226>.
- [11] X. Yan, Y. Zhang, Functional properties and promising applications of high entropy alloys, Scr. Mater. 187 (2020) 188–193, <https://doi.org/10.1016/j.scriptamat.2020.06.017>.
- [12] B.S. Murty, J.W. Yeh, S. Ranganathan, Chapter 8 - structural properties, in: B. S. Murty, J.W. Yeh, S. Ranganathan (Eds.), High Entropy Alloys, Butterworth-Heinemann, Boston, 2014, pp. 133–148, <https://doi.org/10.1016/B978-0-12-800251-3.00008-0>.
- [13] S.P. Wang, J. Xu, TiZrNbTaMo high-entropy alloy designed for orthopedic implants: As-cast microstructure and mechanical properties, Mater. Sci. Eng. C. 73 (2017) 80–89, <https://doi.org/10.1016/j.msec.2016.12.057>.
- [14] M. Todai, T. Nagase, T. Hori, A. Matsugaki, A. Sekita, T. Nakano, Novel TiNbTaZrMo high-entropy alloys for metallic biomaterials, Scr. Mater. 129 (2017) 65–68, <https://doi.org/10.1016/j.scriptamat.2016.10.028>.
- [15] A. Motallebzadeh, N.S. Peighambarioust, S. Sheikh, H. Murakami, S. Guo, D. Canadinc, Microstructural, mechanical and electrochemical characterization of TiZrTaHfNb and Ti1.5ZrTa0.5Hf0.5Nb0.5 refractory high-entropy alloys for biomedical applications, Intermetallics 113 (2019) 106572, <https://doi.org/10.1016/j.intermet.2019.106572>.
- [16] T. Hori, T. Nagase, M. Todai, A. Matsugaki, T. Nakano, Development of non-equiatomic Ti-Nb-Ta-Zr-Mo high-entropy alloys for metallic biomaterials, Scr. Mater. 172 (2019) 83–87, <https://doi.org/10.1016/j.scriptamat.2019.07.011>.
- [17] T. Nagase, M. Todai, T. Hori, T. Nakano, Microstructure of equiatomic and non-equiatomic Ti-Nb-Ta-Zr-Mo high-entropy alloys for metallic biomaterials Microstructure of equiatomic and non-equiatomic Ti-Nb-Ta-Zr-Mo high-entropy alloys for metallic biomaterials, J. Alloy. Compd. 753 (2018) 412–421, <https://doi.org/10.1016/j.jallcom.2018.04.082>.
- [18] T. Nagase, Y. Iijima, A. Matsugaki, K. Ameyama, T. Nakano, Design and fabrication of Ti-Zr-Hf-Cr-Mo and Ti-Zr-Hf-Co-Cr-Mo high-entropy alloys as metallic biomaterials, Mater. Sci. Eng. C 107 (2020) 110322, <https://doi.org/10.1016/j.msec.2019.110322>.
- [19] Y. Iijima, T. Nagase, A. Matsugaki, P. Wang, K. Ameyama, T. Nakano, Design and development of Ti-Zr-Hf-Nb-Ta-Mo high-entropy alloys for metallic biomaterials, Mater. Des. 202 (2021) 109548, <https://doi.org/10.1016/j.matdes.2021.109548>.
- [20] J. Shittu, M. Pole, I. Cockerill, M. Sadeghilardjani, L.V.K. Reddy, G. Manivasagam, H. Singh, H.S. Grewal, H.S. Arora, S. Mukherjee, Biocompatible High Entropy Alloys with Excellent Degradation Resistance in a Simulated Physiological Environment, ACS Appl. Bio Mater. 3 (2020) 8890–8900, <https://doi.org/10.1021/acsabm.0c01181>.
- [21] W. Yang, S. Pang, Y. Liu, Q. Wang, P.K. Liaw, T. Zhang, Design and properties of novel Ti-Zr-Hf-Nb-Ta high-entropy alloys for biomedical applications, Intermetallics 141 (2022) 107421, <https://doi.org/10.1016/j.intermet.2021.107421>.
- [22] M. Akmal, Systematic study of (MoTa)xNbTiZr medium- and high-entropy alloys for biomedical implants- In vivo biocompatibility examination, J. Mater. Sci. 9 (2021).
- [23] A. Chavan, S. Mandal, M. Roy, Cobalt free refractory high entropy alloys for total joint arthroplasty: in-vitro wear, corrosion and cytocompatibility evaluation, J. Alloy. Compd. 938 (2023) 168499, <https://doi.org/10.1016/j.jallcom.2022.168499>.
- [24] S.-P. Wang, J. Xu, (TiZrNbTa)-Mo high-entropy alloys: dependence of microstructure and mechanical properties on Mo concentration and modeling of solid solution strengthening, Intermetallics 95 (2018) 59–72, <https://doi.org/10.1016/j.intermet.2018.01.017>.
- [25] N. Hua, W. Wang, Q. Wang, Y. Ye, S. Lin, L. Zhang, Q. Guo, J. Brechtl, P.K. Liaw, Mechanical, corrosion, and wear properties of biomedical Ti-Zr-Nb-Ta-Mo high entropy alloys, J. Alloy. Compd. 861 (2021) 157997, <https://doi.org/10.1016/j.jallcom.2020.157997>.
- [26] Y. Tong, L. Bai, X. Liang, Y. Chen, Z. Zhang, J. Liu, Y. Li, Y. Hu, Influence of alloying elements on mechanical and electronic properties of NbMoTaWX (X = Cr, Zr, V, Hf and Re) refractory high entropy alloys, Intermetallics 126 (2020) 106928, <https://doi.org/10.1016/j.intermet.2020.106928>.

- [27] C. Li, Y. Ma, X. Yang, M. Hou, New TiTaNbZrMo high-entropy alloys for metallic biomaterials, *Mater. Res. Express* 8 (2021) 105403, <https://doi.org/10.1088/2053-1591/ac2f0b>.
- [28] Y. Gao, L. Qiao, D. Wu, Y. Zhang, Y. Zou, First principle calculation of the effect of Cr, Ti content on the properties of VMoNbTaWMx (M = Cr, Ti) refractory high entropy alloy, *Vacuum* 179 (2020) 109459, <https://doi.org/10.1016/j.vacuum.2020.109459>.
- [29] Y.L. Hu, L.H. Bai, Y.G. Tong, D.Y. Deng, X.B. Liang, J. Zhang, Y.J. Li, Y.X. Chen, First-principle calculation investigation of NbMoTaW based refractory high entropy alloys, *J. Alloy. Compd.* 827 (2020) 153963, <https://doi.org/10.1016/j.jallcom.2020.153963>.
- [30] S. Lin, Y. Yao, Z. Yao, Y. Liu, Y. Liu, P. Zhang, W. Qin, X. Wu, Construction of FeCrVTiMo high-entropy alloys with enhanced mechanical properties based on electronegativity difference regulation strategy, *J. Alloy. Compd.* 957 (2023) 170431, <https://doi.org/10.1016/j.jallcom.2023.170431>.
- [31] A. Sharma, P. Singh, T. Kirk, V.I. Levitas, P.K. Liaw, G. Balasubramanian, R. Arroyave, D.D. Johnson, Pseudoelastic deformation in Mo-based refractory multi-principal element alloys, *Acta Mater.* 220 (2021) 117299, <https://doi.org/10.1016/j.actamat.2021.117299>.
- [32] G. Kim, H. Diao, C. Lee, A.T. Samaei, T. Phan, M. de Jong, K. An, D. Ma, P.K. Liaw, W. Chen, First-principles and machine learning predictions of elasticity in severely lattice-distorted high-entropy alloys with experimental validation, *Acta Mater.* 181 (2019) 124–138, <https://doi.org/10.1016/j.actamat.2019.09.026>.
- [33] Y. Wang, M. Yan, Q. Zhu, W.Y. Wang, Y. Wu, X. Hui, R. Otis, S.-L. Shang, Z.-K. Liu, L.-Q. Chen, Computation of entropies and phase equilibria in refractory V-Nb-Mo-Ta-W high-entropy alloys, *Acta Mater.* 143 (2018) 88–101, <https://doi.org/10.1016/j.actamat.2017.10.017>.
- [34] F. Tian, L.K. Varga, N. Chen, J. Shen, L. Vitos, Ab initio design of elastically isotropic TiZrNbMoV high-entropy alloys, *J. Alloy. Compd.* 599 (2014) 19–25, <https://doi.org/10.1016/j.jallcom.2014.01.237>.
- [35] U. Bhandari, H. Ghadimi, C. Zhang, F. Gao, S. Yang, S. Guo, Computational exploration of biomedical HfNb_{0.5}Ta_{0.5}Zr and Hf_{0.5}Nb_{0.5}Ta_{0.5}Ti_{1.5}Zr refractory high-entropy alloys, *Mater. Res. Express* 8 (2021) 096534, <https://doi.org/10.1088/2053-1591/ac1d65>.
- [36] N.E. Koval, J.I. Juaristi, R. Díez Muiño, M. Alducin, Elastic properties of the TiZrNbTaMo multi-principal element alloy studied from first principles, *Intermetallics* 106 (2019) 130–140, <https://doi.org/10.1016/j.intermet.2018.12.014>.
- [37] W. Ching, P.K. Liaw, Fundamental electronic structure and multiaatomic bonding in 13 biocompatible high-entropy alloys, *Npj Computational Materials* (n.d.) 1–10, <https://doi.org/10.1038/s41524-020-0321-x>.
- [38] S. Schönecker, X. Li, D. Wei, S. Nozaki, H. Kato, L. Vitos, X. Li, Harnessing elastic anisotropy to achieve low-modulus refractory high-entropy alloys for biomedical applications, *Mater. Des.* 215 (2022) 110430, <https://doi.org/10.1016/j.matdes.2022.110430>.
- [39] J.H. Dai, W. Li, Y. Song, L. Vitos, Theoretical investigation of the phase stability and elastic properties of TiZrHfNb-based high entropy alloys, *Mater. Des.* 182 (2019) 108033, <https://doi.org/10.1016/j.matdes.2019.108033>.
- [40] Y.X. Ye, B.L. Musico, Z.Z. Lu, L.B. Xu, Z.F. Lei, V. Keppens, H.X. Xu, T.G. Nieh, Evaluating elastic properties of a body-centered cubic cubic NbHfZrTi high-entropy alloy – A direct comparison between experiments and ab initio calculations, *Intermetallics* 109 (2019) 167–173, <https://doi.org/10.1016/j.intermet.2019.04.003>.
- [41] A. van de Walle, Multicomponent multisublattice alloys, nonconfigurational entropy and other additions to the Alloy Theoretic Automated Toolkit, *Calphad* 33 (2009) 266–278, <https://doi.org/10.1016/j.calphad.2008.12.005>.
- [42] A.D. Corso, *dalcorso/thermo_pw*, (2022). (https://github.com/dalcorso/thermo_pw) (accessed October 17, 2022).
- [43] P. Giannozzi, S. Baroni, N. Bonini, M. Calandra, R. Car, C. Cavazzoni, D. Ceresoli, G.L. Chiarotti, M. Cococcioni, I. Dabo, A. Dal Corso, S. de Gironcoli, S. Fabris, G. Fratesi, R. Gebauer, U. Gerstrmann, C. Gougoussis, A. Kokalj, M. Lazzeri, L. Martin-Samos, N. Marzari, F. Mauri, R. Mazzarello, S. Paolini, A. Pasquarello, L. Paulatto, C. Sbraccia, S. Scandolo, G. Sclauzero, A.P. Seitsonen, A. Smogunov, P. Umari, R.M. Wentzcovitch, QUANTUM ESPRESSO: a modular and open-source software project for quantum simulations of materials, *J. Phys. Condens. Matter* 21 (2009) 395502, <https://doi.org/10.1088/0953-8984/21/39/395502>.
- [44] 2016Cover Image, Volume 37, Issue 11, Journal of Compu.pdf, (n.d.). (https://schmelting.ac.rwth-aachen.de/coph/download/Maintz_et_al-2016-Journal_of_Computational_Chemistry.pdf) (Accessed 17 October 2022).
- [45] CALPHAD: Calculation of Phase Diagrams - a Comprehensive Guide, Elsevier, 1998. [https://doi.org/10.1016/S1470-1804\(98\)X8001-6](https://doi.org/10.1016/S1470-1804(98)X8001-6).
- [46] J.-O. Andersson, T. Helander, L. Höglund, P. Shi, B. Sundman, Thermo-Calc & DICTRA, computational tools for materials science, *Calphad* 26 (2002) 273–312, [https://doi.org/10.1016/S0364-5916\(02\)00037-8](https://doi.org/10.1016/S0364-5916(02)00037-8).
- [47] Z. Leong, U. Ramamurti, T.L. Tan, Microstructural and compositional design principles for Mo-V-Nb-Ti-Zr multi-principal element alloys: a high-throughput first-principles study, *Acta Mater.* 213 (2021) 116958, <https://doi.org/10.1016/j.actamat.2021.116958>.
- [48] C. Nataraj, E.J.L. Borda, A. van de Walle, A. Samanta, A systematic analysis of phase stability in refractory high entropy alloys utilizing linear and non-linear cluster expansion models, *Acta Mater.* 220 (2021) 117269, <https://doi.org/10.1016/j.actamat.2021.117269>.
- [49] A. van de Walle, P. Tiwary, M. de Jong, D.L. Olmsted, M. Asta, A. Dick, D. Shin, Y. Wang, L.-Q. Chen, Z.-K. Liu, Efficient stochastic generation of special quasirandom structures, *Calphad* 42 (2013) 13–18, <https://doi.org/10.1016/j.calphad.2013.06.006>.
- [50] F.T. Tahir, M. Husain, N. Sfina, A.A. Rached, M. Khan, N. Rahman, Probing the physical properties for prospective high energy applications of QMnF₃ (Q = Ga, In) halide perovskites compounds employing the framework of density functional theory, *RSC Adv.* 13 (2023) 18788–18798, <https://doi.org/10.1039/D3RA02878J>.
- [51] M. Jamal, S. Jalali Asadabadi, I. Ahmad, H.A. Rahnamaye Aliabad, Elastic constants of cubic crystals, *Comput. Mater. Sci.* 95 (2014) 592–599, <https://doi.org/10.1016/j.commatsci.2014.08.027>.
- [52] -Efficient machine-learning model for fast assessment of elastic properties of high-entropy alloys, *Acta Materialia* 232 (2022) 117924. <https://doi.org/10.1016/j.actamat.2022.117924>.
- [53] S. Qiu, N. Miao, J. Zhou, Z. Guo, Z. Sun, Strengthening mechanism of aluminum on elastic properties of NbVtZr high-entropy alloys, *Intermetallics* 92 (2018) 7–14, <https://doi.org/10.1016/j.intermet.2017.09.003>.
- [54] P.E. Blöchl, Projector augmented-wave method, *Phys. Rev. B* 50 (1994) 17953–17979, <https://doi.org/10.1103/PhysRevB.50.17953>.
- [55] J.P. Perdew, K. Burke, M. Ernzerhof, Generalized gradient approximation made simple, *Phys. Rev. Lett.* 77 (1996) 3865–3868, <https://doi.org/10.1103/PhysRevLett.77.3865>.
- [56] E. Osei-Ayemang, G. Balasubramanian, Surface oxidation mechanism of a refractory high-entropy alloy, *Npj Mater. Degrad.* 3 (2019) 20, <https://doi.org/10.1038/s41529-019-0082-5>.
- [57] V.L. Deringer, A.L. Tchougréeff, R. Dronskowski, Crystal orbital hamiltonian population (cohph) analysis as projected from plane-wave basis sets, *J. Phys. Chem. A* 115 (2011) 5461–5466, <https://doi.org/10.1021/jp202489s>.
- [58] J. Normand, R. Moriche, C. García-Garrido, R.E. Sepúlveda Ferrer, E. Chicardi, Development of a TiNbTaMoZr-based high entropy alloy with low Young's modulus by mechanical alloying route, *Metals* 10 (2020) 1463, <https://doi.org/10.3390/met10111463>.
- [59] L. Shao, M. Yang, L. Ma, B.-Y. Tang, Effect of Ta and Ti content on high temperature elasticity of HfNbZrTa_{1-x}Tix refractory high-entropy alloys, *Int. J. Refrac. Met. Hard Mater.* 95 (2021) 105451, <https://doi.org/10.1016/j.ijrmhm.2020.105451>.
- [60] L. Raman, A. Anupam, G. Karthick, C.C. Berndt, A.S.M. Ang, S.V.S. Narayana Murty, D. Fabijanic, B.S. Murty, R.S. Kottada, Strengthening mechanisms in CrMoNbTiW refractory high entropy alloy, *Mater. Sci. Eng. A* 819 (2021) 141503, <https://doi.org/10.1016/j.msea.2021.141503>.
- [61] H. Liu, L. Liu, C. Xin, Effect of alloying elements on the structure and mechanical properties of NbMoTaWX (X = Cr, V, Ti, Zr, and Hf) refractory high-entropy alloys, *AIP Adv.* 11 (2021) 025044, <https://doi.org/10.1063/5.0038405>.
- [62] Y. Liu, Z. Yao, P. Zhang, S. Lin, M. He, S. Lu, X. Wu, Enhanced strength without sacrificing ductility in FeCrMnVSi high entropy alloys via controlling the ratio of metallic to covalent bonding, *Mater. Des.* 225 (2023) 111565, <https://doi.org/10.1016/j.matdes.2022.111565>.
- [63] P. Singh, A. Sharma, A.V. Smirnov, M.S. Diallo, P.K. Ray, G. Balasubramanian, D. D. Johnson, Design of high-strength refractory complex solid-solution alloys, *Npj Comput. Mater.* 4 (2018) 16, <https://doi.org/10.1038/s41524-018-0072-0>.
- [64] S. Guo, C. Ng, J. Lu, C.T. Liu, Effect of valence electron concentration on stability of fcc or bcc phase in high entropy alloys, *J. Appl. Phys.* 109 (2011) 103505, <https://doi.org/10.1063/1.3587228>.
- [65] ASM Handbook - Vol 03 - Alloy Phase Diagrams (500s).pdf, (n.d.).
- [66] H. Ikehata, N. Nagasako, T. Furuta, A. Fukumoto, K. Miwa, T. Saito, First-principles calculations for development of low elastic modulus Ti alloys, *Phys. Rev. B* 70 (2004) 174113, <https://doi.org/10.1103/PhysRevB.70.174113>.
- [67] J. Wang, S. Bai, Y. Tang, S. Li, X. Liu, J. Jia, Y. Ye, L. Zhu, Effect of the valence electron concentration on the yield strength of Ti-Zr-Nb-V high-entropy alloys, *J. Alloy. Compd.* 868 (2021) 159190, <https://doi.org/10.1016/j.jallcom.2021.159190>.
- [68] I. Lobzenko, Y. Shihara, H. Mori, T. Tsuru, Influence of group IV element on basic mechanical properties of BCC medium-entropy alloys using machine-learning potentials, *Comput. Mater. Sci.* 219 (2023) 112010, <https://doi.org/10.1016/j.commatsci.2023.112010>.
- [69] W. Yang, S. Pang, Y. Liu, Q. Wang, P.K. Liaw, T. Zhang, Design and properties of novel Ti-Zr-Hf-Nb-Ta high-entropy alloys for biomedical applications, *Intermetallics* 141 (2022) 107421, <https://doi.org/10.1016/j.intermet.2021.107421>.
- [70] M.M. Khrushev, Principles of abrasive wear, *Wear* 28 (1974) 69–88, [https://doi.org/10.1016/0043-1648\(74\)90102-1](https://doi.org/10.1016/0043-1648(74)90102-1).